

Ultrafast laser direct hard-mask writing for high efficiency c-Si texture designs

Kitty Kumar¹, Kenneth K.C. Lee², Jun Nogami¹, Peter R. Herman², and Nazir P. Kherani^{1,2,a}

¹ Department of Materials Science and Engineering, 184 College Street, Toronto, Ontario, M5S 3E4, Canada

² Department of Electrical and Computer Engineering, 10 King's College Rd. Toronto, Ontario, M5S 3G4, Canada

Received: 5 October 2012 / Received in final form: 31 January 2013 / Accepted: 21 February 2013

Published online: 22 March 2013

© Kumar et al., published by EDP Sciences, 2013

Abstract This study reports a high-resolution hard-mask laser writing technique to facilitate the selective etching of crystalline silicon (c-Si) into an inverted-pyramidal texture with feature size and periodicity on the order of the wavelength which, thus, provides for both anti-reflection and effective light-trapping of infrared and visible light. The process also enables engineered positional placement of the inverted-pyramid thereby providing another parameter for optimal design of an optically efficient pattern. The proposed technique, a non-cleanroom process, is scalable for large area micro-fabrication of high-efficiency thin c-Si photovoltaics. Optical wave simulations suggest the fabricated textured surface with 1.3 μm inverted-pyramids and a single anti-reflective coating increases the relative energy conversion efficiency by 11% compared to the PERL-cell texture with 9 μm inverted pyramids on a 400 μm thick wafer. This efficiency gain is anticipated to improve further for thinner wafers due to enhanced diffractive light trapping effects.

1 Introduction

A major trend driving the development of low-cost high-efficiency c-Si based photovoltaics is a reduction in material cost through the use of thinner wafers [1,2]. However, thin Si wafers do not readily lend themselves to high-efficiency photovoltaic devices owing to large penetration depth of infrared wavelengths. Therefore, along with surface reflection reduction, an effective light-trapping scheme is imperative for the use of thinner wafers in photovoltaic devices.

In present commercial solar cells, 160–200 μm thick c-Si wafers are chemically etched in hot potassium hydroxide (KOH) solution to form random pyramids of few to ten microns in size on the wafer surface [3] that reduces the surface reflection by promoting multiple bounces of the incident light. However, such texture with large-scale pyramids is not appropriate for thin wafers due to the high Si consumption during etching and little to no optical diffraction for efficient light-trapping. In contrast, optical modeling has shown reduced surface reflection and strong diffraction for effective light-trapping in thin wafers only when grating textures are reduced to feature size comparable with the wavelength [4]. Although various textures consisting of rods [5,6], cones [6], inverted-pyramids [7], holes (honey-comb structure) [8], grooves [9], etc. have

been applied in different lattice configurations and with different pitches to decrease reflectivity. Inverted-pyramid texture and honey-comb texture are the most preferred in practice due to the simple, cost-effective wet chemical processes that are widely available for Si wafers in industry [10]. Further, assessment by Zhao et al. [11] favours an inverted-pyramidal texture over a honeycomb pattern of holes. In addition, the exposed (111) planes in the inverted-pyramidal texture can be readily passivated, a critical requirement for efficient collection of photogenerated carriers. Photolithography has produced inverted-pyramidal texture with 9 μm feature size that demonstrates record energy conversion efficiency in solar cells [12], while further improvements are anticipated from nano-imprint and colloidal lithography [7] that pushes the inverted-pyramid size to sub-micron scale for thin wafers. These methods have been researched extensively and have yet to be adopted for mass production.

In this paper, we present an alternative approach of patterning silicon with inverted pyramids using a non-cleanroom laser direct hard-mask writing technique. The process avails femtosecond laser interaction for blistering (Fig. 1a) and catapulting (Fig. 1b) of thin-film dielectric coatings on c-Si (100) to form a high-resolution hard-mask on c-Si which in turn facilitates chemical etching of Si into inverted-pyramidal structure (Fig. 1c). The technique enables inverted-pyramidal texturing of Si with flexible pattern designs, thus exploiting the low reflection, high

^a e-mail: kherani@ecf.utoronto.ca

diffractive light-trapping capability and passivation benefits of such texture. While femtosecond lasers have been used to texturize c-Si with chemical assistance [13], the produced ‘black’ silicon has significant structural damage that prevents passivation and decreases carrier lifetime. Alternatively, femtosecond lasers have been applied to SiO_x thin films on c-Si to form micro-blisters [13, 14] and induce catapulting which we extend to SiN_x and further exploit here to form a high resolution hard mask for KOH etching.

2 Optimization of the texturing process

Various thicknesses of SiO_x and SiN_x films were grown to serve as hard masks (100 nm to 300 nm for SiO_x; 20 nm to 266 nm for SiN_x) for alkaline etching. The SiN_x layer was grown by plasma enhanced chemical vapor deposition (PECVD) on single-side polished *p*-type (100) c-Si wafers of 400 μm thickness in a PlasmaLab 100 PECVD system (Oxford Instruments) at 300 °C and 650 mT chamber pressure using a gas mixture of 5% silane in nitrogen (400 sccm), ammonia (20 sccm) and pure nitrogen (600 sccm). The deposition was carried out at the rate of 14 nm/minute by using alternating combinations of high frequency (13.56 MHz) plasma for 13 s and low frequency (100 KHz) plasma for 7 s successively. The RF power was set to 50 W and 40 W for high and low frequencies, respectively. For SiO_x, the PECVD procedure was modified to 1000 mT chamber pressure and a gas mixture of 5% silane in nitrogen (170 sccm) and nitrous oxide (710 sccm). The deposition was carried out at the rate of 55 nm/minute by using 30W RF power. Owing to the high etching rate of 18 nm/min of SiO_x in KOH compared with 1.2 nm/min for SiN_x, a minimum of 100 nm thick SiO_x and 20 nm thick SiN_x is required for hard-masking Si during KOH etching. Thus, a systematic study on laser-induced blistering and catapulting was carried out on 100 nm to 300 nm thick SiO_x and 20 nm to 266 nm thick SiN_x film to establish fluence thresholds and exposure windows that produced the smallest ablation craters in hard mask with high reproducibility and minimal collateral damage to expose Si for alkaline etching. The femtosecond fiber laser (FCPA μJewel D-400-VR, IMRA) output was frequency doubled to 522 nm via second harmonic generation, and applied at 100 kHz pulse repetition rate to avoid cumulative heating effects by such rapidly arriving laser pulses. The beam was linearly polarized and of 170 fs pulse duration. By monitoring the back reflection on a CCD camera, a plano-convex lens of 8mm focal length (5724-H-A New Focus) focused the Gaussian-shaped laser beam to a diffraction-limited spot size of 1.25 μm diameter (1/e²) precisely onto the sample surface that was mounted on a XY motorized stages (ABL1000, Aerotech). A linear polarizer and waveplate power attenuator varied the laser pulse energy between 0.2 and 1.25 nJ to drive different levels of surface modification in hard masks of various thicknesses. Additional laser processing details are provided in reference [15]. Further, the smallest craters in all the films were tested for effective anisotropic etching in 30 wt% aqueous

solution of KOH maintained at 60 °C using a two-step procedure. First, the sample was etched for 30 s, and then cleaned and washed in DI water followed by nitrogen drying. Second, the sample was etched again over a variable time to yield a high-fidelity inverted-pyramid structure. The first step served to mainly remove ablation debris.

The fluence threshold for blistering and catapulting of SiN_x was found to increase strongly from 0.29 J/cm² and 0.45 J/cm², respectively, for a 20 nm thick film to 0.67 J/cm² and 1.02 J/cm², respectively for a 266 nm thick film. However, the values modulate with varying Fabry-Pérot interference effects as the optical film thickens. Over this film thickness range, the minimum ablation crater diameter was found to increase monotonically from 0.6 μm to ~2 μm. Generally, higher fluence was necessary to generate larger internal ablation pressure to delaminate and lift thicker films, but at the cost of creating larger diameter craters in the c-Si substrate. The observed fluence thresholds and the ablation crater diameters were nearly identical in SiO_x films in comparison with SiN_x films of the same thickness, and are in accord with the results reported for 147 nm SiO_x films [13]. During KOH etching, the smallest ablation craters in ≥100 nm thick SiN_x/SiO_x films did not etch to form inverted-pyramids. This is attributed to the high fluence (≥0.96 J/cm²) used to delaminate ≥100 nm thick films that crystallographically damages the underlying Si and thus rendering it unetchable in KOH [16]. The results show that the thinnest possible dielectric film is favoured to yield the smallest ablation crater diameter with minimum Si damage. Hence, a 20 nm SiN_x film was deemed optimal for creating the smallest possible mask aperture with sufficient thickness to resist KOH etching.

The blister dynamics observed in 20 nm SiN_x with increasing laser fluence was similar to that reported for a 100 nm SiO_x film [17]. The blister grows in diameter until a threshold for the perforation of the blister is reached at which point a nano-hole is formed, followed by mechanical ejection of the blistered SiN_x film at higher fluences, leaving behind approximately a 50 nm deep crater in the underlying Si substrate. Figure 2a shows scanning electron micrographs (SEMs) of this sequence beginning with the threshold for blister formation (0.29 J/cm²), and following with the threshold for perforating the blister with a nanohole (0.31 J/cm²), the collapse of a blister with a nanohole (0.41 J/cm²), the catapulting threshold fluence for mechanically ejecting the blister (0.45 J/cm²), and the catapulted blister at a fluence above the threshold (0.49 J/cm²). The corresponding atomic force micrographs and line profiles of this morphology are shown in Figures 2b and 2c, respectively, while Figure 2d shows SEMs of the corresponding features after KOH etching for 2.5 min (step1: 30 s, step2: 2 min). The blistered SiN_x layer (intact, perforated and collapsed) was found to protect the underlying Si from KOH etching whereas the unprotected Si crater formed due to a blister catapulting (≥0.45 J/cm²) resulted in typical inverted-pyramid structure after KOH treatment. Further, the ablation crater diameter and the effect of KOH etching was, comprehensively, examined over a broad range

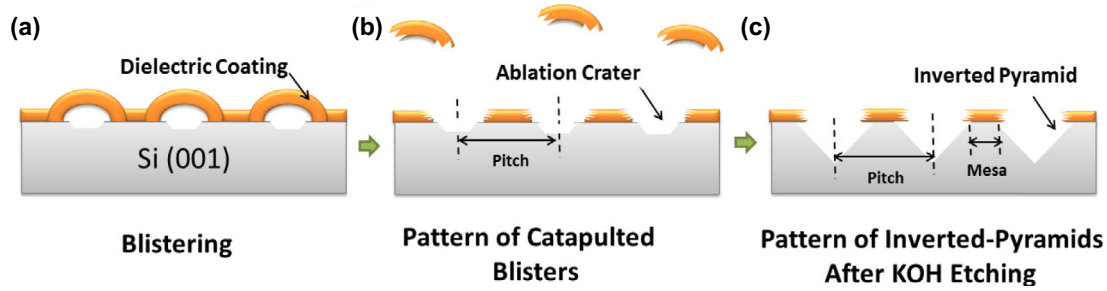


Fig. 1. A schematic illustrating (a) blistering of a dielectric coating upon interaction with femtosecond pulses, (b) catapulting of the blisters at higher laser fluence to form a pattern of shallow ablation craters in c-Si, and (c) the resulting inverted-pyramid structure following KOH etching.

of laser exposure conditions to determine the smallest possible inverted-pyramid structure that could be reproducibly formed with the tightest packing density and the results are summarized in Figure 2e. The graph shows the crater diameter and the resulting inverted-pyramid width after etching in KOH for 2.5 min to increase from $0.6 \mu\text{m}$ and $1.13 \mu\text{m}$, respectively, at 0.43 J/cm^2 to $1.25 \mu\text{m}$ and $1.31 \mu\text{m}$, respectively, at 0.53 J/cm^2 fluence. The degree of undercutting increases dramatically as the fluence decreases towards the catapulting threshold, below which only blistering is observed. This is attributed to the decrease in laser-induced Si damage at low fluence. The undercutting was essential to etch beyond the laser damage zone in the c-Si surface to expose damage free (111) planes. The increasing damage apparent in the SEM images (Fig. 2e inset) with increasing laser fluence required longer etching times to compensate for damage but with the trade-off of forming larger sized inverted-pyramid structures. The smallest ($1.13 \mu\text{m}$) clean inverted-pyramid was reproducibly formed at 0.45 J/cm^2 whereas a $1.07 \mu\text{m}$ wide inverted-pyramid was formed at 0.43 J/cm^2 with only 33% reproducibility.

A high density grid of inverted-pyramids was next investigated using the optimized 0.45 J/cm^2 fluence exposure. At 100 kHz repetition rate, the pitch (Λ) of craters along the scanning direction (x) was examined over a range of $\Lambda_x = 1.2$ to $1.5 \mu\text{m}$ by varying the scan speed between 120 to 150 mm/s, while line-to-line offsets (y -direction) of $\Lambda_y = 1.2$ to $2 \mu\text{m}$ were tested to create tightly packed arrays with minimum collateral damage. The densest packing was found for $1.5 \mu\text{m}$ spacing in both directions, yielding the grid of craters shown in Figure 3a that etched into a high-fidelity array of inverted-pyramids seen in top and cross-sectional views (inset) in Figure 3b. In the array of ablation craters produced at optimized fluence, the inverted-pyramid size can be varied from $1.13 \mu\text{m}$ to $1.3 \mu\text{m}$ by increasing the KOH etching time from 2.5 to 5 min, leaving a 370 nm to 200 nm wide flat mesa, respectively, between the inverted-pyramids. A further increase in the inverted-pyramid size would lead to occasional over-etching that manifests in the fusion of neighboring pyramids. Larger area SEM observation of the inverted-pyramidal texture (Fig. 3c) did not reveal any pyramid defects over our whole sample set ($\sim 14,000$ holes

viewed) in spite of a non-cleanroom processing environment, suggesting a high reproducibility of the devised technique with less than 1 defect per 10^4 holes.

3 Flexibility offered by the texturing process

The method offers the advantage of independently varying pattern pitches in x - and y -directions with the help of computer-controlled motion stages, as illustrated in Figure 3d. Also, the laser exposure can be modulated during wafer scanning with the help of an acoustic optical modulator (AOM) driven by position-synchronized output (PSO) of the motion stages to create patterns of inverted-pyramids; this is illustrated through the creation of the University of Toronto crest which is shown in SEM and optical images (Figs. 3e and 3f, respectively). A micro-pattern of the inverted-pyramid structure is shown in Figure 3e (inset). In the optical image, the bare silicon appears bright, whereas the texturized regions appear dark, demonstrating their strong optical anti-reflection property.

4 Optical performance

After optimization, $2 \text{ cm} \times 2 \text{ cm}$ textures with inverted pyramids of $1.13 \mu\text{m}$ and $1.3 \mu\text{m}$ sizes arrayed at our highest pitch density ($\Lambda_x = \Lambda_y = 1.5 \mu\text{m}$) were fabricated to measure the anti-reflection efficacy and the effect of mesa width on the anti-reflectance efficacy of the textures. Figures 4a and 4b show total reflectance at normal incidence and specular reflectance at different angles of incidence, respectively, together with the total reflectance spectrum measured for a bare Si wafer. With $1.13 \mu\text{m}$ wide inverted-pyramids, the surface reflectance was reduced to an average of 18.6% compared with untextured silicon which reflects 34.7% of incident light in the wavelength range 400 nm–1000 nm. For $1.3 \mu\text{m}$ pyramids, the reflectance was reduced to 13.6% due to the 42% decrease in the width of mesas. For the same sample, the total reflectance was further reduced to 4% with the addition of an incompletely optimized 70 nm thick SiN_x anti-reflective coating (ARC). Calculated optical reflectivity curves are also plotted for the cases of $1.3 \mu\text{m}$ inverted-pyramids (with 200 nm

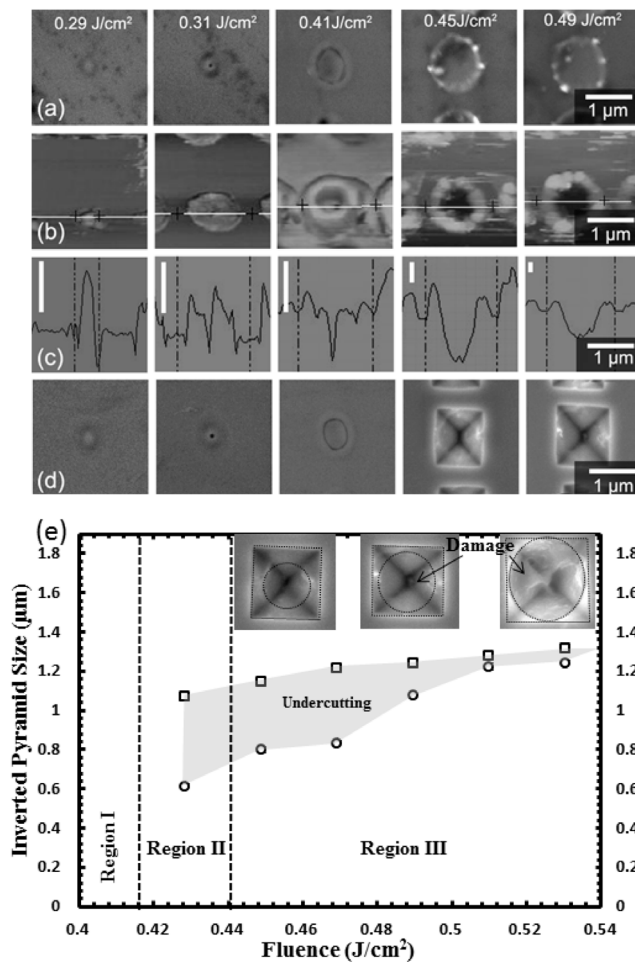


Fig. 2. (a) SEM images of surface modifications in a 20 nm SiN_x film on c-Si as a function of laser fluence. Corresponding atomic force micrographs and line profiles of the features are shown in (b) and (c), respectively. The vertical scale bar is 20 nm in each panel of (c). (d) Shows post-etching SEM micrographs of the morphology shown in (a), when etched in KOH for 2.5 min. The ablation crater diameter (circular marker (o)) and the inverted-pyramid size (square marker (\square)) observed after 2.5 min KOH etching are shown in (e) together with select SEM images as a function of fluence. The mask aperture and the inverted pyramid are outlined by a dashed circle and a square, respectively, in each of the SEM images. Fluence zones for blistering (Region I) and low (Region II) and high (Region III) reproducible ejection are identified.

mesas) and the untextured Si surface. Optical wave analysis based on the scattering matrix method [18] was used to simulate the total optical reflectance at normal incidence over the 280 nm–1000 nm spectrum. Reflectivity of the inverted pyramid texture on a 400 μm thick polished silicon wafer was calculated for a set pitch of 1.5 μm and inverted pyramid size of 1.13 μm and 1.3 μm . For 70 nm thick SiN_x PECVD antireflective coating, the optical constants were experimentally obtained by ellipsometry. The simulated and measured curves match in the case of untextured Si, whereas a slight incongruity is seen for the 1.3 μm inverted-pyramid texture; this deviation

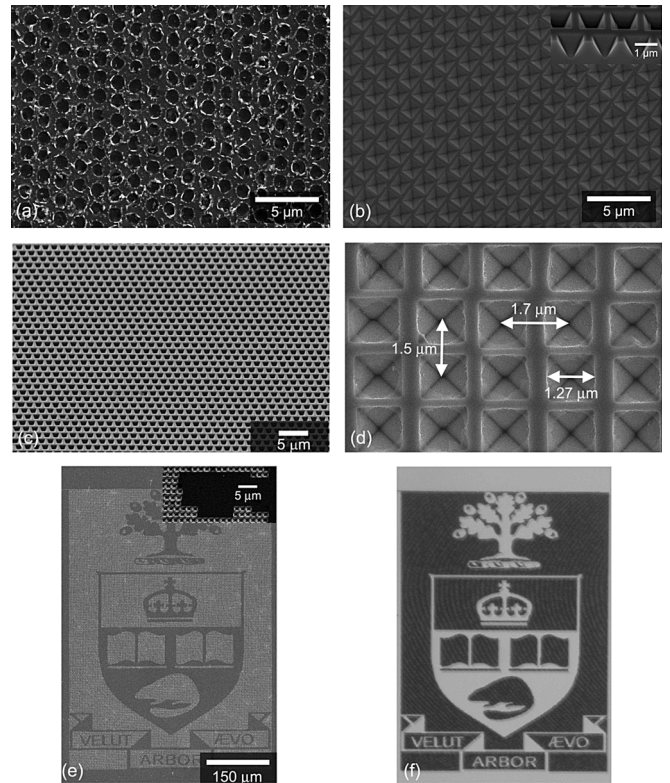


Fig. 3. (a) Top view of a Si wafer with a grid of catapulted blisters at 1.5 μm spacing. KOH etching results in a clean array of 1.3 μm inverted-pyramids seen in top and cross-sectional views (inset) (b) and in a large area oblique-view (c). The defect-free texture indicates the high reproducibility offered by the devised technique. (d) Shows an array of 1.27 μm sized inverted-pyramids placed at $A_x = 1.5 \mu\text{m}$ and $A_y = 1.7 \mu\text{m}$. (e) SEM image of a University of Toronto crest micro-patterned with inverted-pyramid structure shown in (e) (inset) demonstrates the capability of the technique to selectively texture areas, leaving untextured planar areas for front contacts. The patterned areas appear bright in this image. (f) The optical image of the crest demonstrates the strong anti-reflective effect in the textured areas.

is possibly due to our theoretical assumption of a square grid arrangement of inverted pyramids, whereas the laboratory sample had skewed alignment of adjacent rows due to the limited control available in the motion stages. The average specular reflectance over 280 nm–1000 nm for the AR coated (70 nm thick SiN_x deposited by PECVD) texture with 1.13 μm inverted-pyramids lies below 2% for incidence angles of 8° to 40° and rapidly increases to 3%, 4.6% and 7.9% for incident angles of 48°, 56° and 64°, respectively, indicating better optical performance when compared with the grid-less PERL-cell [19] that is also plotted in Figure 4b for comparison.

5 Efficiency calculations

Given the strong anti-reflective characteristics observed in the present inverted-pyramid structures, it is instructive to simulate the cell efficiency as a function of

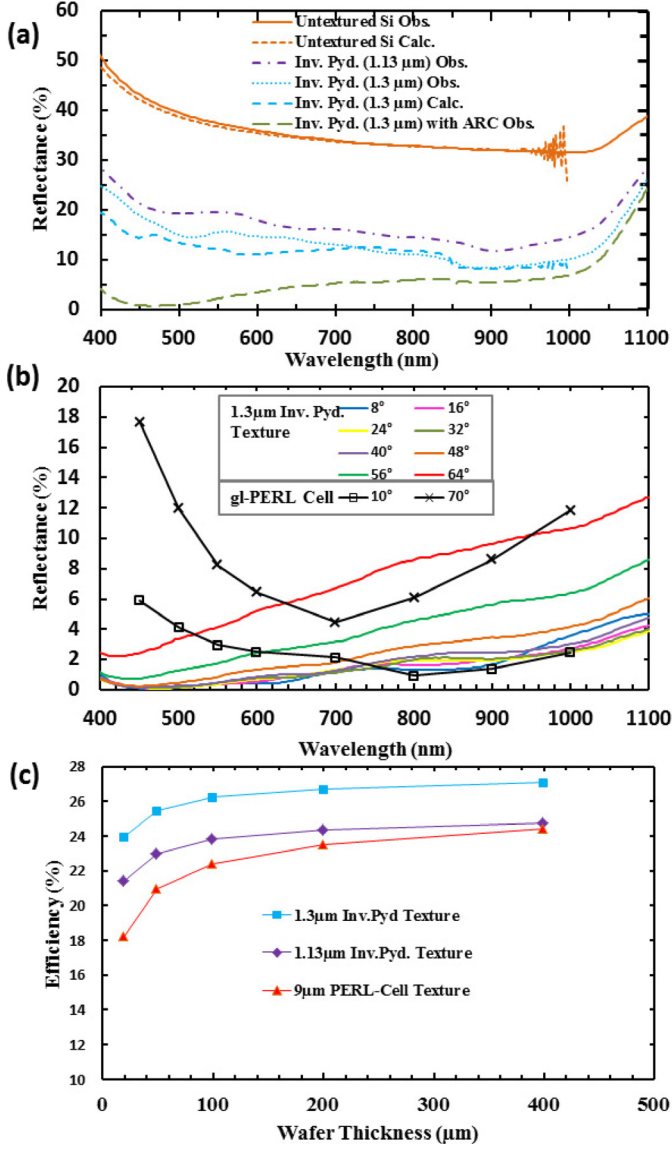


Fig. 4. (a) Experimental (solid lines) and simulated (dashed lines) total reflectance spectra at normal incidence from fabricated samples (1.13 μm and 1.3 μm inverted-pyramids) and bare silicon as a function of wavelength. (b) Measured specular reflectance spectra from 1.3 μm inverted pyramid texture coated with a 70 nm thick SiN_x ARC and from a grid-less PERL-cell with dual layer ARC [19] for the various incidence angles shown. (c) Predicted efficiency of a solar cell with the presently fabricated (1.13 and 1.3 μm inverted-pyramid) and the PERL-cell textures at various wafer thicknesses. A 70 nm thick PECVD deposited SiN_x ARC is considered in efficiency calculations.

wafer thickness for the textures fabricated in this study and the 9 μm inverted-pyramidal texture with $\Lambda_x = \Lambda_y = 10 \mu\text{m}$ that was used in the grid-less PERL-cell. Inverted pyramids were placed on the light facing side of the wafer, etched in to a polished silicon wafer of a given thickness. A 70 nm thick SiN_x ARC and a perfect back reflector were assumed for the front and rear surfaces, respectively, in

both cases. For efficiency calculations, the total number of photons absorbed in the solar cell N_{ph} was calculated by integrating absorption of AM1.5 solar radiation over the wavelength range of 280 nm–1000 nm. Consistent with Feng et al. [20], a collection efficiency of 85% was assumed. The short circuit current was given by $J_{sc} = 0.85 \times eN_{ph}$, where e is the electronic charge. The open circuit voltage was obtained from $V_{oc} = (kT/e) \ln(J_{sc}/J_o + 1)$, where k is the Boltzmann constant, $T = 300 \text{ K}$, and J_o is the reverse bias saturation current. Given that the smallest J_o value of about $10^{-15} \text{ A cm}^{-2}$ [21] for Si at 300 K, here we use $J_o = 1.5 \times 10^{-15} \text{ A cm}^{-2}$. A fill factor of 80% was assumed, representing an achievable value for a well-designed photovoltaic device operating at the maximum power point [21]. Finally, the solar cell efficiency was expressed as $\eta = 0.8 \times J_{sc} \times V_{oc}/P_{AM1.5}$, where $P_{AM1.5} = 0.1 \text{ W cm}^{-2}$ is the incident power of AM1.5 solar radiation.

The simulation results (Fig. 4c) show a moderate efficiency gain of 2.7% and 0.4% for the 1.3 μm and 1.13 μm inverted-pyramids, respectively, in relation to the 24.4% for the PERL-cell texture in the case of a 400 μm thick wafer. Smaller mesas are clearly favoured as expected, while the smaller pyramids on the size scale of optical wavelengths benefit from reduced reflection due to the graded refractive index effect. However, much stronger enhancement is found in thinner wafers. Efficiency gain of 5.7% is obtained in the case of 1.3 μm sized inverted pyramids on 20 μm thin wafers in relation to the 18.2% PERL-cell texture, due to the enhanced light trapping from the larger diffraction angles possible in the smaller periodic surface structure that directs the weakly absorbing infrared light laterally and thus resulting in a marked increase in performance in such thin wafers. Further, the 1.3 μm texture effectively etches less silicon for a given wafer thickness compared to the PERL-cell texture, and hence it provides more silicon for light absorption.

6 Results and discussion

We have demonstrated a simple and versatile hard-mask writing technique for inverted-pyramid texturing of c-Si with texture feature size and pitch on the order of wavelength. The technique uses individual laser pulses to define the pattern of catapulting blisters in a 20 nm-thin SiN_x layer to expose the underlying c-Si with minimal laser damage, which is then effectively etched with KOH to form a high fidelity inverted-pyramidal texture. The technique offers control over the periodicity through the use of computer controlled motion stages whereas feature size can be modulated by varying laser fluence or alternatively by chemical etching time. It also offers precise control of the patterned areas. Further, the proposed patterning technique along with the feature size of the order of wavelength leads to minimal removal of silicon ($\sim 1 \mu\text{m}$) and consequently has beneficial implications for high-efficiency ultra-thin ($\sim 20 \mu\text{m}$) silicon PV where excess Si for etching

is not available. A relative Si material savings of $\sim 80\%$ is anticipated when using our inverted pyramids of $1.3\ \mu\text{m}$ size in comparison with the $9\ \mu\text{m}$ PERL-cell inverted pyramids.

Detailed optical wave calculations on a $400\ \mu\text{m}$ thick wafer suggest relative efficiency enhancement of 11% and 1.4% for the $1.3\ \mu\text{m}$ and $1.13\ \mu\text{m}$ inverted-pyramids, respectively, when compared with the PERL-cell texture of $9\ \mu\text{m}$ inverted-pyramids. Light trapping is not imperative in thick wafers and hence, the predicted enhancement in $400\ \mu\text{m}$ thick wafer is mainly due to the graded refractive index effectively formed by the inverted-pyramids of the order of wavelength that couples more light into the Si substrate thereby increasing the cell efficiency. Smaller mesas result in stronger enhancement as expected. However, in thin wafers the amount of light trapping significantly affects the cell efficiency. Specifically, for a $20\ \mu\text{m}$ thick wafer a much stronger enhancement of 31.6% and 17.7% is calculated in the case of $1.3\ \mu\text{m}$ and $1.13\ \mu\text{m}$ inverted-pyramids, respectively, relative to the PERL-cell texture. This enhancement in efficiency is due to two factors. First, due to the diffraction of light from the fabricated textures that directs the weakly absorbing infrared light laterally which is effectively absorbed in such thin wafers. Second, $1.3\ \mu\text{m}$ inverted pyramid texture etches $\sim 80\%$ less Si and hence offers more material for light absorption relative to the PERL-cell texture.

In the present study, catapulted blisters were formed at the rate of $10^5\ \text{s}^{-1}$ with $0.55\ \text{mW}$ laser power. The current development of $\geq 100\ \text{W}$ femtosecond lasers together with multi-lens focusing arrays suggests a $\sim 2 \times 10^5$ fold increase in the processing rate, i.e., 2×10^{10} blisters per second, equivalent to $200\ \text{cm}^2$ area production per second that can meet the requirements of current c-Si solar cell manufacturing processes. With further advances in lasers and beam delivery methods the proposed approach has the potential of becoming a practical texturing technique for high-efficiency thin c-Si photovoltaics.

This work was supported by the Natural Sciences and Engineering Research Council of Canada, the Ontario Research Fund – Research Excellence program, and the University of Toronto.

References

1. K.A. Munzer, K.T. Holdermann, R.E. Schlosser, S. Sterk, *IEEE Trans. Electron Devices* **46**, 2055 (1999)
2. C.T.M. Group, International Technology Roadmap for Photovoltaics (ITRPEV.net) Results 2010 2, (2011)
3. D. Munoz, P. Carreras, J. Escarre, D. Ibarz, S. Martin de Nicolas, C. Voz, J.M. Asensi, J. Bertomeu, *Thin Solid Films* **517**, 3578 (2009)
4. H. Sai, Y. Kanamori, K. Arafune, Y. Ohshita, M. Yamaguchi, *Prog. Photovolt. Res. Appl.* **15**, 415 (2007)
5. C.H. Sun, W.-L. Min, N.C. Linn, P. Jiang, B. Jiang, *J. Vac. Sci. Technol. B* **27**, 1043 (2009)
6. C.M. Hsu, S.T. Connor, M.X. Tang, Y. Cui, *Appl. Phys. Lett.* **93**, 133109 (2008)
7. C.H. Sun, W.L. Min, N.C. Linn, P. Jiang, B. Jiang, *Appl. Phys. Lett.* **91**, 231105 (2007)
8. G. Kumaravelu, M.M. Alkai, A. Bittar, in *Proc. of the 29th IEEE Photovoltaic Specialists Conference, New Orleans, 2002*, pp. 258–261
9. Y. Kanamori, M. Sasaki, K. Hane, *Opt. Lett.* **24**, 1422 (1999)
10. M. Moynihan, *CircuiTree* **22**, 16 (2009)
11. J. Zhao, A. Wang, Martin A. Green, F. Ferrazza, *Appl. Phys. Lett.* **73**, 1991 (1998)
12. M.A. Green, K. Emery, Y. Hishikawa, W. Warta, E.D. Dunlop, *Prog. Photovolt. Res. Appl.* **19**, 565 (2011)
13. B.R. Tull, J.E. Carey, E. Mazur, J.P. McDonald, S.M. Yalisove, *MRS Bull.* **31**, 626 (2006)
14. J.P. McDonald, A.A. McClelland, Y.N. Picard, S.M. Yalisove, *Appl. Phys. Lett.* **86**, 264103 (2005)
15. K. Kumar, K.K.C. Lee, P.R. Herman, J. Nogami, N.P. Kherani, *Appl. Phys. Lett.* **101**, 222106 (2012)
16. T. Rublack, M. Schade, M. Muchow, H.S. Leipner, G. Seifert, *J. Appl. Phys.* **112**, 023521 (2012)
17. T. Rublack, S. Hartnauer, P. Kappe, C. Swiatkowski, G. Seifert, *Appl. Phys. A* **103**, 43 (2011)
18. A. Chutinan, N.P. Kherani, S. Zukotynski, *Opt. Express* **17**, 8871 (2009)
19. A. Parretta, A. Sarno, P. Tortora, H. Yakubu, P. Maddalena, J. Zhao, A. Wang, *Opt. Commun.* **172**, 139 (1999)
20. N.-N. Feng, J. Michel, J. Michel, L. Zeng, J. Liu, C.-Y. Hong, L.C. Kimerling, X. Duan, *IEEE Trans. Electron Devices* **54**, 1926 (2007)
21. S.M. Sze, *Physics of semiconductor devices*, 2nd edn. (Wiley, New York, 1981)

Cite this article as: Kitty Kumar, Kenneth K.C. Lee, Jun Nogami, Peter R. Herman, Nazir P. Kherani, Ultrafast laser direct hard-mask writing for high efficiency c-Si texture designs, *EPJ Photovoltaics* **4**, 45101 (2013).